New Journal of Physics

The open access journal at the forefront of physics

PAPER

Control of electron beam polarization in the bubble regime of laser-wakefield acceleration

H C Fan[1], X Y Liu[1], X F Li[2,3,4,*] ⬧, J F Qu[1], Q Yu[5] ⬧, Q Kong[1,*] ⬧, S M Weng[3,4] ⬧, M Chen[3,4] ⬧, M Büscher[6,7] ⬧, P Gibbon[2,8] ⬧, S Kawata[9] ⬧ and Z M Sheng[3,4,10,11] ⬧

[1] Key Laboratory of Nuclear Physics and Ion-Beam Application (MOE), Institute of Modern Physics, Department of Nuclear Science and Technology, Fudan University, Shanghai 200433, People's Republic of China
[2] Institute for Advanced Simulation, Jülich Supercomputing Centre, Forschungszentrum Jülich, 52425 Jülich, Germany
[3] Key Laboratory for Laser Plasmas (MoE), School of Physics and Astronomy, Shanghai Jiao Tong University, Shanghai 200240, People's Republic of China
[4] Collaborative Innovation Centre of IFSA, Shanghai Jiao Tong University, Shanghai 200240, People's Republic of China
[5] State Key Laboratory of High Field Laser Physics, Shanghai Institute of Optics and Fine Mechanics, Chinese Academy of Sciences, Shanghai 201800, People's Republic of China
[6] Peter Grünberg Institut (PGI-6), Forschungszentrum Jülich, Wilhelm-Johnen-Str. 1, 52425 Jülich, Germany
[7] Institut für Laser- und Plasmaphysik, Heinrich-Heine-Universität Düsseldorf, Universitätsstr. 1, 40225 Düsseldorf, Germany
[8] Centre for Mathematical Plasma Astrophysics, Katholieke Universiteit Leuven, 3000 Leuven, Belgium
[9] Graduate School of Engineering, Utsunomiya University, Utsunomiya 321-8585, Japan
[10] SUPA, Department of Physics, University of Strathclyde, Glasgow G4 0NG, United Kingdom
[11] Tsung-Dao Lee Institute, Shanghai Jiao Tong University, Shanghai 200240, People's Republic of China
[*] Authors to whom any correspondence should be addressed.

E-mail: xia.li@fz-juelich.de, xiaofengli@sjtu.edu.cn and qkong@fudan.edu.cn

Abstract

Electron beam polarization in the bubble regime of the interaction between a high-intensity laser and a longitudinally pre-polarized plasma is investigated by means of the Thomas–Bargmann–Michel–Telegdi equation. Using a test-particle model, the dependence of the accelerated electron polarization on the bubble geometry is analysed in detail. Tracking the polarization dynamics of individual electrons reveals that although the spin direction changes during both the self-injection process and acceleration phase, the former has the biggest impact. For nearly spherical bubbles, the polarization of electron beam persists after capture and acceleration in the bubble. By contrast, for aspherical bubble shapes, the electron beam becomes rapidly depolarized, and the net polarization direction can even reverse in the case of a oblate spheroidal bubble. These findings are confirmed via particle-in-cell simulations.

Contents

1. Introduction

Laser wakefield acceleration (LWFA) has made remarkable progress since it was first proposed by Tajima and Dawson in 1979 [1] and experimentally realized through the rapid advancement of laser technology via

chirped-pulse amplification [2]. Since then, improved understanding of various schemes such as plasma beat wave acceleration [3], multiple laser pulses [4, 5], and self-modulated LWFA [6] have contributed to a series of milestones. Of particular note is the generation of quasimonoenergetic electron beams in the bubble regime [7], which triggered significant experimental progress and widespread interest [8–10]. In recent years, applications of wakefield acceleration have been actively pursued, such as synchrotron radiation sources [11, 12] and polarized particle beams [13–15].

Spin-polarized particle beams are widely used in nuclear and particle physics to study the interaction and structure of matter, and to test the standard model of particle physics [16, 17]. In particular, the structure of subatomic particles like protons or neutrons can be explored to get further insights into quantum chromodynamics [18] or to probe the nuclear spin structure [19]. Additionally, polarized particle beams are advantageous to achieve a deeper understanding of nuclear reactions [20], to investigate symmetry violations, to measure quantum numbers of new particles [16, 21–23], or to investigate molecular dynamics [24, 25]. In 2019, An *et al* proposed to map electromagnetic field structures of plasmas by using a spin-polarized relativistic electron beam [26]. In contrast, a first polarization measurement of few-MeV laser accelerated protons reported a negative result, i.e. no polarization build-up during the acceleration process with an unpolarized foil target [27]. Recently, polarized multi-GeV proton beams produced by ultra-intense laser interaction with pre-polarized target were studied via simulations [28]. At present, the preparation of polarized electron beams mainly relies on spontaneous polarization in the magnetic fields of storage rings due to the emission of spin-flip synchrotron radiation, i.e. the well-known Sokolov–Ternov effect [29, 30]. This technique requires conventional particle accelerators that are typically very large in scale and budget [29].

The acceleration of polarized electron beams by means of laser-driven acceleration promises to be cost-efficient and highly effective. Despite many advances mostly on the theoretical side, several principal issues need to be addressed, for example: (i) is it possible to alter the polarization of an initially unpolarized target through interaction with relativistic laser pulses [31–35]? or (ii) are the spins so inert during the short acceleration period that a pre-polarized target is required [13, 14, 36–38]? Following the work by Hützen *et al* [39], Wen *et al* [13] have proposed to generate high-current polarized electron beams in the interaction of an ultra-intense laser pulse with a pre-polarized gas plasma, which is produced through photo-dissociation by a circularly polarized ultra-violet (UV) laser pulse [40]. The work of Vieira *et al* showed that spin is depolarized mainly in the injection phase [41].

Previous works show that the distribution of the electromagnetic fields is affected by the accelerating bubble geometry [42–44]. It is thus likely that the self-injection process can be affected by the bubble shape [45, 46]. Moreover, the work of Qu *et al* [47] indicates that the frequency of THz radiation generated by the shell electrons also depends on the bubble shape. In this paper, the evolution of the electron beam polarization injected into various shapes of ellipsoidal bubbles is discussed in detail, and it is found that the polarization of electron beams can be controlled by adjusting the bubble geometry. The results of our analysis are highly relevant to experimental implementations of polarized electron beams, such as those planned at the European EuPRAXIA facility [48].

2. Test-particle model

By choosing appropriate laser and plasma parameters, different shaped wakefield bubbles can be achieved [45]. A series of 2.5D particle-in-cell (PIC) simulation with the code EPOCH [49] was carried out to analyse the bubble geometry. The laser propagates in the x-direction with linear polarization in the y-direction and a Gaussian envelope

$$E = E_0 \frac{w_0}{w(x)} \exp\left(-\frac{y^2 + z^2}{w^2(x)}\right) \exp\left(-\frac{(kx - \omega t)^2}{(0.5\tau)^2}\right) \cos(\varphi), \tag{1}$$

where, $w(x) = w_0[1 + (x - x_0)^2/z_R^2]^{0.5}$, with laser waist $w_0 = 10\lambda$, pulse duration $\tau = 21$ fs, laser intensity $a_0 = eE_0/m_e\omega c = 20$ and wavelength $\lambda = 800$ nm. The $x_0 = 30\lambda$ is the position of the laser waist, and $z_R = \pi w_0^2/\lambda$ is the Rayleigh length. The vacuum length was 30λ and the laser beam was focused at the left edge of plasma. The simulation box is $140\lambda(x) \times 100\lambda(y)$ with resolution $dx = \lambda/32$ and $dy = 5\,dx$. There were 16 pseudo-particles per cell. We define the aspect ratio $\eta = R_\perp/R_\parallel$ to describe the shape of bubble, where $R_\parallel$ and $R_\perp$ are the longitudinal and transverse radii respectively. Different $R_\parallel$ and $R_\perp$ can be obtained by changing the plasma density for the same laser system [45]. The simulation result shows that the bubble shape changes from prolate to oblate spheroid with increasing plasma density. Following this definition, $\eta < 1$ indicates a prolate spheroid, $\eta = 1$ indicates a sphere, and $\eta > 1$ indicates an oblate spheroid. For an

initial plasma density of $n_0 = 0.011 n_c$, we find that $R_{\parallel} = 14.38\lambda$ and $R_{\perp} = 13.13\lambda$. Consequently, the aspect ratio $\eta = 0.91 < 1$, represents a prolate spheroidal bubble.

The electromagnetic field distribution in a spherical bubble has already been theoretically and numerically studied [50–52]. Based on the work of Li *et al* [44], the electromagnetic field of an ellipsoidal bubble can be written as

$$E_x = \frac{\eta^2}{\eta^2(1 - v_b^2) + 2}\xi, \tag{2a}$$

$$E_y = \frac{2 - \eta^2 v_b^2}{2\eta^2(1 - v_b^2) + 4}y, \tag{2b}$$

$$E_z = \frac{2 - \eta^2 v_b^2}{2\eta^2(1 - v_b^2) + 4}z, \tag{2c}$$

$$B_x = 0, \tag{2d}$$

$$B_y = \frac{v_b\eta^2}{2\eta^2(1 - v_b^2) + 4}z, \tag{2e}$$

$$B_z = -\frac{v_b\eta^2}{2\eta^2(1 - v_b^2) + 4}y, \tag{2f}$$

where $\xi = x - v_b t$, $v_b = \sqrt{1 - \gamma_b^{-2}}$ is the bubble phase velocity and $\gamma_b = 0.45\sqrt{n_c/n_0}$ [50, 53]. To confine the field distribution inside the bubble, a modified factor $f(r) = \left[\tanh(R_{\parallel}/d - r/d) + 1\right]/2$ was used, $r = \sqrt{\xi^2 + (y^2 + z^2)/\eta^2}$ and d is the width of the electron sheath. In this work, $d = 0.5$ was used. Here, we used dimensionless units, by normalizing the length to k_p, the velocity to c, the electron density to n_0, the electric field to $m_e c\omega_p/e$, and the magnetic field to $m_e\omega_p/e$.

Initially, the electron is at rest in front of the bubble with a position (x_0, y_0). Considering a fully polarized plasma, the electron spin at initial time is aligned with in the bubble propagation direction (x). To follow the trajectory of an electron in the bubble, a fourth-order Runge–Kutta method was adopted to numerically solve the relativistic Newton–Lorentz equation, $dP/dt = -e\left[E + (P/\gamma) \times B\right]$, where $\gamma = 1/\sqrt{1 - v^2/c^2}$ is the relativistic factor. Meanwhile, the spin precession of an electron in the electromagnetic field was calculated according to the Thomas–Bargmann–Michel–Telegdi (TBMT) equation [29] $ds/dt = (\mathbf{\Omega}_T + \mathbf{\Omega}_a) \times s$ with
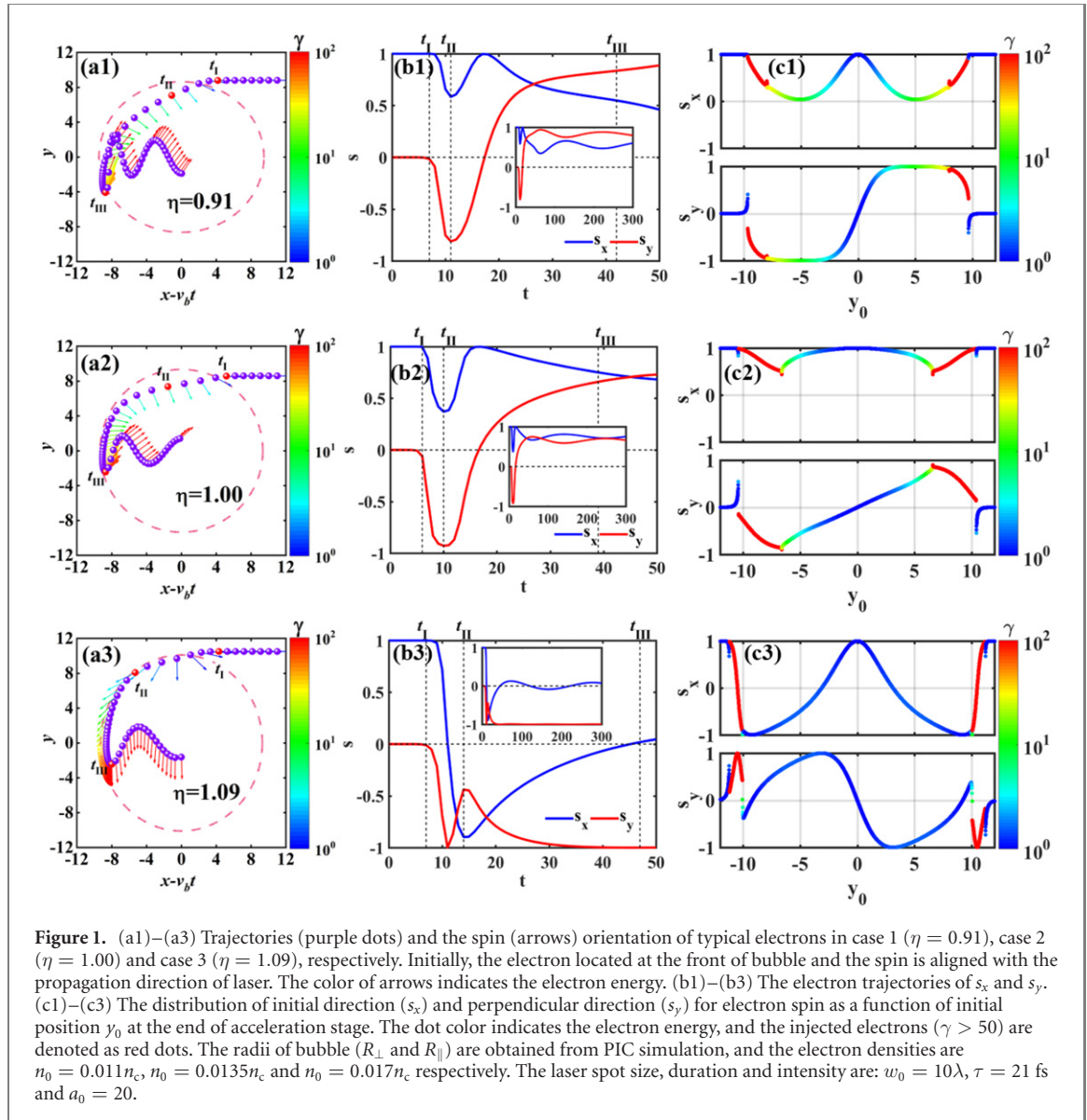
$$\mathbf{\Omega}_T = \frac{e}{m_e}\left(\frac{1}{\gamma}\mathbf{B} - \frac{1}{\gamma + 1}\frac{\mathbf{v}}{c^2} \times \mathbf{E}\right), \tag{3a}$$

$$\mathbf{\Omega}_a = a_e\frac{e}{m_e}\left(\mathbf{B} - \frac{\gamma}{\gamma + 1}\frac{\mathbf{v}}{c^2}(\mathbf{v} \cdot \mathbf{B}) - \frac{\mathbf{v}}{c^2} \times \mathbf{E}\right), \tag{3b}$$

where $a_e \approx 1.16 \times 10^{-3}$ is the anomalous magnetic moment of the electron and the spin is normalized to $|s| = 1$. The Boris-rotation method was adopted to numerically solve the TBMT equation [54].
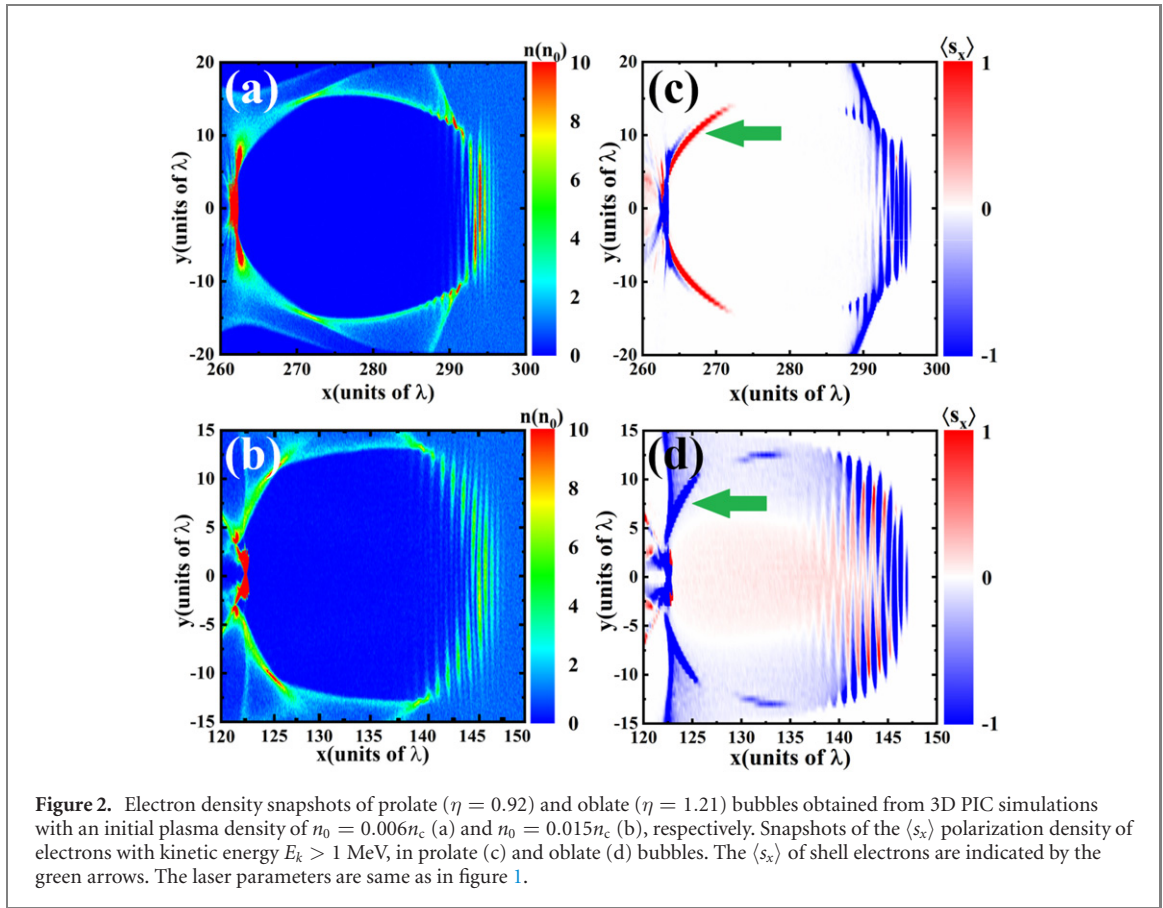
Owing to the azimuthal symmetry of the wake magnetic field, the electron orbit and spin can be placed in the same plane [13, 50], so for simplicity the *XY* plane was adopted for this calculation. The simulation results of three typical cases are displayed in figure 1. The aspect ratio of these bubbles were $\eta = 0.91$ in case 1, $\eta = 1.00$ in case 2 and $\eta = 1.09$ in case 3, representing prolate spheroidal, spherical and oblate spheroidal bubbles, respectively. The trajectory and the spin orientation of a typical electron are presented in figures 1(a1)–(a3). The motion of electrons can be divided into four stages: (i) $t < t_I$, the electron does not feel the bubble field; (ii) $t_I < t < t_{II}$, the electron is located on the bubble shell and its spin rotates clockwise, such that s_y decreases from 0 to almost -1 as shown in figure 1(b1); (iii) $t_{II} < t < t_{III}$, the electron reaches the tail of the bubble and its spin rotates counter-clockwise, and s_y increases as revealed in figure 1(b1); (iv) $t > t_{III}$, the electron is captured in the bubble and its spin procession slows down.

The degree of electron spin precession differs for the three cases. The electrons can stay longer in the second stage with increasing η, which means that the degree of clockwise rotation is largest for case 3 $(\eta > 1)$, where s_x approaches -1 as shown as figure 1(b3). During the third stage, the degree of spin precession in the three cases is also different. In case 1 $(\eta < 1)$ and case 2 $(\eta = 1)$, s_x increases to 1 (its initial value) and decreases afterwards, while s_y changes from negative to positive. In case 3 $(\eta > 1)$, the counter-clockwise spin precession is significantly smaller. Thus, s_x increases from -1 to a value near 0 and s_y remains negative.

Figure 1. (a1)–(a3) Trajectories (purple dots) and the spin (arrows) orientation of typical electrons in case 1 ($\eta = 0.91$), case 2 ($\eta = 1.00$) and case 3 ($\eta = 1.09$), respectively. Initially, the electron located at the front of bubble and the spin is aligned with the propagation direction of laser. The color of arrows indicates the electron energy. (b1)–(b3) The electron trajectories of s_x and s_y. (c1)–(c3) The distribution of initial direction (s_x) and perpendicular direction (s_y) for electron spin as a function of initial position y_0 at the end of acceleration stage. The dot color indicates the electron energy, and the injected electrons ($\gamma > 50$) are denoted as red dots. The radii of bubble ($R_\perp$ and $R_\parallel$) are obtained from PIC simulation, and the electron densities are $n_0 = 0.011 n_c$, $n_0 = 0.0135 n_c$ and $n_0 = 0.017 n_c$ respectively. The laser spot size, duration and intensity are: $w_0 = 10\lambda$, $\tau = 21$ fs and $a_0 = 20$.

During the fourth stage $t > t_{\mathrm{III}}$ the electrons remain in the acceleration phase and oscillate around the laser axis. The s_x and s_y values oscillate around their values at $t = t_{\mathrm{III}}$, as shown in the inset of figures 1(b1)–(b3). Compared to the strong precession during the earlier stages, this spin variation can be ignored. This means that the spin procession for electrons *mainly occurs during self-injection*, and does not change significantly thereafter in the acceleration stage, and this result is consistent with the study of Wen *et al* [13]. When the electron arrives at the centre of bubble, the acceleration process is terminated and the spin direction is similar to its value at $t = t_{\mathrm{III}}$, as revealed as insets of figures 1(b1)–(b3). At this time, the final spin orientation is forward in case 1 ($\eta < 1$), case 2 ($\eta = 1$) and backward in case 3 ($\eta > 1$). We can thus conclude that the spin precession is strongly affected by the bubble geometry. Moreover, during the electron injection, the clockwise spin rotation during the second stage is partly balanced by the counter-clockwise rotation of stage three. As a consequence, a particular ellipsoidal bubble shape can be chosen for which the electron spins can be restored to their initial orientation at $t = t_{\mathrm{III}}$ and maintain dynamic stability over the acceleration phase.

The net polarization of a particle beam is defined as $P = \sqrt{\langle s_x \rangle^2 + \langle s_y \rangle^2 + \langle s_z \rangle^2}$, where $\langle s_i \rangle$ is the average value in each direction. This definition is a statistical average for an electron bunch. An accelerated electron beam can be mimicked by changing the initial position y_0 for a set of test particles. The trapping cross-section has been studied using the same method in a previous study [45]. The distributions of s_x and s_y as a function of initial position y_0 at the end of acceleration stage are displayed in the figures 1(c1)–(c3). The electrons are also distinguished according to their final energy, denoted by the color scale. In 3D geometry, the injected electrons ($\gamma > 50$) are distributed in a ring. The accelerated electrons (red dots) are distributed from $r_{\min}$ to $r_{\max}$ in these three cases, which means that the electron charge is affected by the

Figure 2. Electron density snapshots of prolate ($\eta = 0.92$) and oblate ($\eta = 1.21$) bubbles obtained from 3D PIC simulations with an initial plasma density of $n_0 = 0.006n_c$ (a) and $n_0 = 0.015n_c$ (b), respectively. Snapshots of the $\langle s_x \rangle$ polarization density of electrons with kinetic energy $E_k > 1$ MeV, in prolate (c) and oblate (d) bubbles. The $\langle s_x \rangle$ of shell electrons are indicated by the green arrows. The laser parameters are same as in figure 1.

bubble geometry. More importantly, the spin direction of the accelerated electrons also depends on the bubble shape. The value of $\langle s_x \rangle$ of the electron beam can be calculated as,
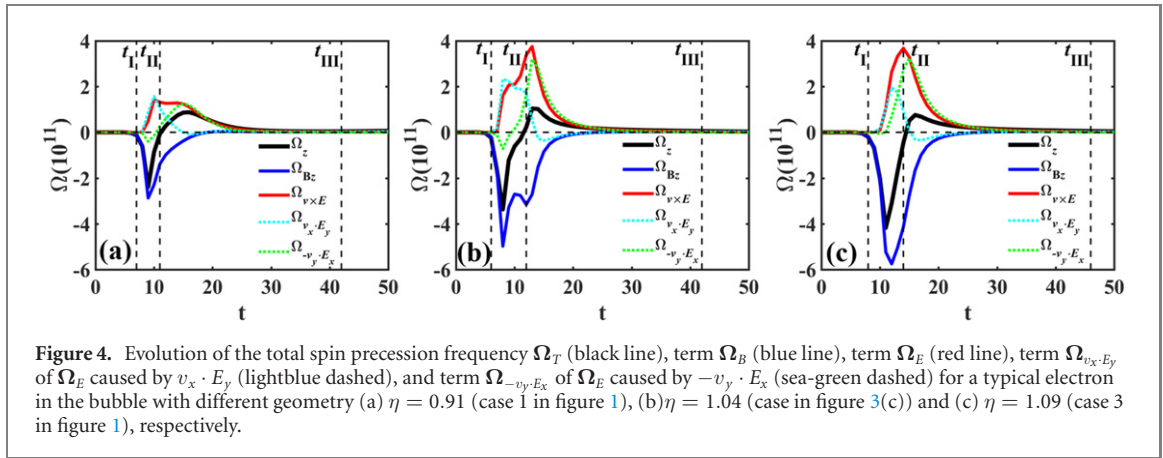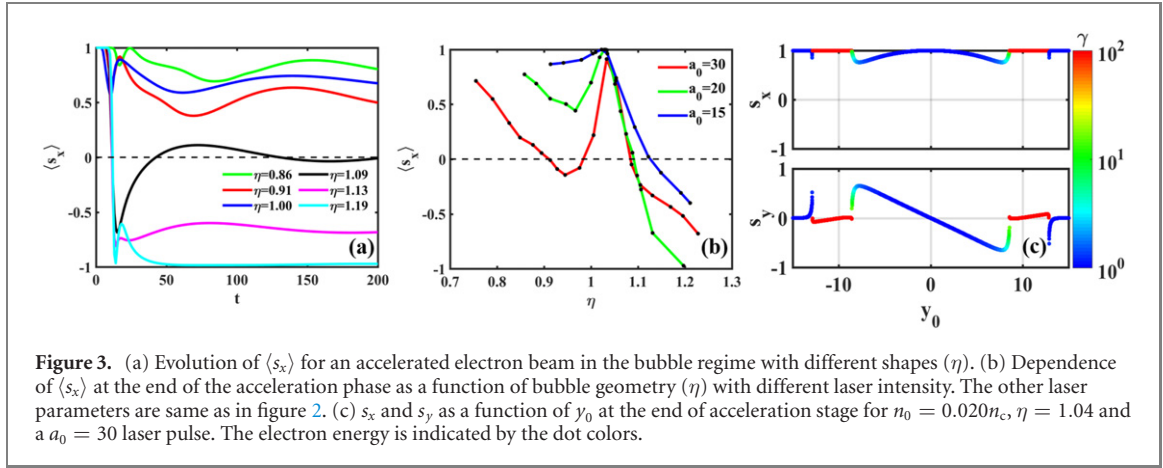
$$\langle s_x \rangle = \frac{\sum_i^N s_{xi}}{N} = \frac{\sum_{r_{\min}}^{r_{\max}} s_{xi} \cdot 2\pi y_0 \delta y_0}{\sum_{r_{\min}}^{r_{\max}} 2\pi y_0 \delta y_0}, \tag{4}$$

with $\delta y_0 = 0.01$ in our simulation. Considering the azimuthal symmetry of the bubble field, we have $\langle s_y \rangle = \langle s_z \rangle = 0$ and $P = |\langle s_x \rangle|$. The polarization amounts to $P = 0.55$, 0.70 and 0.09 for cases 1 ($\eta < 1$), 2 ($\eta = 1$) and 3 ($\eta > 1$) from figure 1, respectively.

3. 3D PIC simulations & discussion

To verify these findings we present results of 3D PIC simulations with a modified version of the EPOCH code [49], in which the TBMT equation for the study of electron and ion spins was implemented [28]. The laser parameters are the same as in figure 1. The initial plasma density is $n_0 = 0.006n_c$ and $n_0 = 0.015n_c$, respectively. The size of the moving window is $60\lambda(x) \times 40\lambda(y) \times 40\lambda(z)$ with resolutions $dx = \lambda/32$ and $dy = dz = 5\,dx$, and 8 pseudo-particles per cell. The pre-polarized plasma can be produced using UV polarization method [40]. While the initial rate of electron polarization in the laser–plasma acceleration structure is not yet totally understood, we assume for simplicity that this is 100%, since we are interested in the evolution of the polarization during the acceleration phase.

As shown as in figures 2(a) and (b), the simulated bubble shapes are prolate ($n_0 = 0.006n_c$) and oblate ($n_0 = 0.015n_c$), respectively. The distribution of $\langle s_x \rangle$ for the two cases are presented in figures 2(c) and (d). The polarization of electrons, located at the tail of bubble, is positive (green arrows) for the prolate bubble ($\eta = 0.92$), while it is negative for the oblate case ($\eta = 1.21$). Thus, the results of our 3D PIC simulations verify the results of the test-particle simulations. Here, the electrons located at the shell of the bubble were analysed because of depolarization process mainly occurs before the electron arrives at the rear wall of the bubble. Moreover, the injection process and the evolution of bubble are also affected by the laser, effects which are not included in the earlier test-particle analysis. To further illustrate how the electron-beam polarization variation depends on the bubble geometry, we did a series of 2.5D PIC simulations with initial plasma densities ranging from $n_0 = 0.005n_c$ to $n_0 = 0.025n_c$ and fixed laser intensity $a_0 = 20$. Other

Figure 3. (a) Evolution of $\langle s_x \rangle$ for an accelerated electron beam in the bubble regime with different shapes (η). (b) Dependence of $\langle s_x \rangle$ at the end of the acceleration phase as a function of bubble geometry (η) with different laser intensity. The other laser parameters are same as in figure 2. (c) s_x and s_y as a function of y_0 at the end of acceleration stage for $n_0 = 0.020n_c$, $\eta = 1.04$ and a $a_0 = 30$ laser pulse. The electron energy is indicated by the dot colors.

Figure 4. Evolution of the total spin precession frequency Ω_T (black line), term Ω_B (blue line), term Ω_E (red line), term $\Omega_{v_x \cdot E_y}$ of Ω_E caused by $v_x \cdot E_y$ (lightblue dashed), and term $\Omega_{-v_y \cdot E_x}$ of Ω_E caused by $-v_y \cdot E_x$ (sea-green dashed) for a typical electron in the bubble with different geometry (a) $\eta = 0.91$ (case 1 in figure 1), (b) $\eta = 1.04$ (case in figure 3(c)) and (c) $\eta = 1.09$ (case 3 in figure 1), respectively.

parameters were the same as in figure 1. The data of bubble geometry were substituted in the single electron dynamic simulations. The evolution curves of $\langle s_x \rangle$ with time are shown in figure 3(a). Here, bubbles with six typical aspect ratios (η) were selected. We found that the $\langle s_x \rangle$ of the electron bunch first decreases then increases in every case, which is similar to the spin dynamics of a single electron—figure 1. When η increases from 0.86 to 0.91, $\langle s_x \rangle$ decreases. When $\eta > 1$, $\langle s_x \rangle$ also decreases with increasing η and even goes negative in an oblate spheroidal bubble. Its value is maximized in a spherical bubble ($\eta = 1$) compared with the two cases with $\eta = 0.91$ and $\eta = 1.09$. This means that the polarization of an accelerated electron bunch can be preserved when the bubble shape is nearly spherical.

In order to check the persistence of this phenomenon, further 2.5D PIC simulations were carried out for different laser parameters. The dependence of $\langle s_x \rangle$ on the various aspect ratios η after acceleration with laser intensities $a_0 = 15, 20, 30$ are presented in figure 3(b). It is found that when the bubble is nearly spherical, the electron-beam depolarization is always minimal. It can even be zero as shown in figure 3(c), where $n_0 = 0.20n_c$, $a_0 = 30$ and $\eta = 1.04$, respectively. In the case of $a_0 \geqslant 20$, the value of $\langle s_x \rangle$ is negatively correlated with η when $\eta < 0.9$, which arises from the smaller number of electrons injected into the bubble.

Finally, the mechanisms governing the spin dynamics in the bubble fields are considered. In figure 4 the evolution of the rotation frequency is analysed for three cases: (a) $\eta = 0.91$ (case 1 in figure 1), (b) $\eta = 1.04$ (case in figure 3(c)), where $\langle s_x \rangle = 0.99$; (c) $\eta = 1.09$ (case 3 in figure 1). The terms of equation (3) are separated into Ω_E and Ω_B for studying their individual contributions to the rotation frequency. Note that $|\Omega_a| \ll |\Omega_T|$, and that Ω_T (solid black line) can be divided to $\Omega_B = eB_z/m_e\gamma$ (solid blue line) and $\Omega_E = -e(v \times E)/[m_e(\gamma + 1)c^2]$ (solid red line).

During the second stage ($t_I < t < t_{II}$), the electrons located near ($\xi \approx 0$, $y \approx r_\perp$) mainly feel E_y and B_z as given in equation (2). Then, Ω_{B_z} and the $v_x \cdot E_y$ term in Ω_E make the largest contribution to Ω_T. Since the electrons cannot obtain enough energy, this results in $|\Omega_{B_z}| > |\Omega_E|$ and the spins rotate clockwise. Assuming a bubble velocity $v_b = 1$, we obtain $B_z \propto (\eta^2 y)/4$ and $E_y \propto [(2 - \eta^2)y]/4$, based on equation (2). With increasing of η, B_z increases and E_y decreases, then Ω_T increases. Meanwhile, the electrons stay longer in this phase, which allows the contribution of B_z to dominate with increasing η, and the degree of clockwise rotation for electron spin is positively correlated with η.

During the third stage ($t_{\mathrm{II}} < t < t_{\mathrm{III}}$), electrons arrive at the tail of bubble ($\xi \approx R_\perp$, $y \approx 0$), where $E_y \approx 0$ and $B_z \approx 0$. Here the electrons mainly feel E_x, then the part of $v_y \cdot E_x$ in $\mathbf{\Omega}_E$ becomes the dominant contribution, which results in counter-clockwise spin rotation. At the tail of bubble $E_x \approx \eta^2 \xi / 2$ under the assumption $v_\mathrm{b} = 1$. Considering $R_\perp$ is similar for bubbles with different shapes and $\xi = R_\parallel$, we obtain $E_x \approx R_\perp^2 / (2R_\parallel)$. With increasing η, $R_\parallel$ decreases and the part of $v_y \cdot E_x$ in $\mathbf{\Omega}_E$ increases. Moreover, considering that the times when electron reach the tail of bubble are different, then the contribution of $\mathbf{\Omega}_{B_z}$ is different for these three cases, which results in similar values of $\mathbf{\Omega}_T$.

For the overall process, the spin rotation is the sum of the clockwise rotation during the second stage and the counter-clockwise rotation during the third stage. With increasing η, the degree of clockwise rotation increases and the degree of counter-clockwise rotation stays roughly constant. Clockwise rotation dominates in the prolate bubble, whereas the counter-clockwise rotation is prevalent in an oblate bubble. More importantly, the two precessions can cancel each other in a bubble with a certain value of η. As shown as figure 4(b), an accelerated electron beam with no net depolarization can be produced when $\eta = 1.04$.

In this work, we investigated the motion of electrons in a pre-polarized plasma, where the initial polarized direction is aligned with the propagation direction of the laser. In this schematic, the s_y and s_z stay zero because of the symmetric precession owing to the azimuthal symmetry of the electromagnetic field in bubble. Although the study of s_x is not a generalized case, the polarization is always preserved for nearly spherical bubble shapes with changing the initial pre-polarized direction.

Previous work has shown that the bubble shape strongly affects the self-injection process, and that this is maximized for near-spherical geometries [45]. The shape can furthermore change over time due to nonlinear propagation beam-loading effects, but fortunately it appears that a spherical bubble will maximize both charge and spin preservation, since the latter is most influence by the period prior to injection. Moreover, the electron polarization also depends on the injection mechanism. Different trajectories of injected electrons cause the disparity of polarization. The further work is necessary to determine which kind of self-injection mechanism is the best choice for a highly polarized electron beam.

4. Conclusion

In summary, the depolarization of accelerated electron bunches has been studied through test-particle dynamics during the interaction of a high-intensity laser with a longitudinally pre-polarized plasma. Spin rotation occurs mainly during the self-injection process. As a consequence, the bubble geometry has a strong influence during this phase, since it determines the electromagnetic field distributions. It is also found that polarization is preserved for nearly spherical bubble shapes. In contrast, non-spherical bubble shapes lead to strong depolarization. These findings should help to choose suitable laser–plasma parameters for producing a polarized electron beam using a pre-polarized plasma. Moreover, the case of a transversal polarization plasma, which is better accessible experimentally, will be investigated in the near future.

Data availability statement

The data generated and/or analysed during the current study are not publicly available for legal/ethical reasons but are available from the corresponding author on reasonable request.

ORCID iDs

X F Li ⬤ https://orcid.org/0000-0002-7710-9800
Q Yu ⬤ https://orcid.org/0000-0001-7223-3469
Q Kong ⬤ https://orcid.org/0000-0001-7476-8571
S M Weng ⬤ https://orcid.org/0000-0001-7746-9462
M Chen ⬤ https://orcid.org/0000-0002-4290-9330
M Büscher ⬤ https://orcid.org/0000-0001-5265-7248
P Gibbon ⬤ https://orcid.org/0000-0002-5540-9626
S Kawata ⬤ https://orcid.org/0000-0002-5830-2234
Z M Sheng ⬤ https://orcid.org/0000-0002-8823-9993

References

[1] Tajima T and Dawson J M 1979 Laser electron accelerator *Phys. Rev. Lett.* **43** 267
[2] Mourou G and Umstadter D 1992 Development and applications of compact high-intensity lasers *Phys. Fluids* B **4** 2315
[3] Rosenbluth M N and Liu C S 1972 Excitation of plasma waves by two laser beams *Phys. Rev. Lett.* **29** 701
[4] Shadwick B A, Schroeder C B and Esarey E 2009 Nonlinear laser energy depletion in laser–plasma accelerators *Phys. Plasmas* **16** 056704
[5] Umstadter D, Esarey E and Kim J 1994 Nonlinear plasma waves resonantly driven by optimized laser pulse trains *Phys. Rev. Lett.* **72** 1224
[6] Leemans W P, Rodgers D, Catravas P E, Geddes C G R, Fubiani G, Esarey E, Shadwick B A, Donahue R and Smith A 2001 Gamma-neutron activation experiments using laser wakefield accelerators *Phys. Plasmas* **8** 2510
[7] Pukhov A and Meyer-ter-Vehn J 2002 Laser wake field acceleration: the highly non-linear broken-wave regime *Appl. Phys.* B **74** 355
[8] Geddes C G R, Toth C, Van Tilborg J, Esarey E, Schroeder C B, Bruhwiler D, Nieter C, Cary J and Leemans W P 2004 High-quality electron beams from a laser wakefield accelerator using plasma-channel guiding *Nature* **431** 538
[9] Mangles S P D *et al* 2004 Monoenergetic beams of relativistic electrons from intense laser–plasma interactions *Nature* **431** 535
[10] Faure J, Glinec Y, Pukhov A, Kiselev S, Gordienko S, Lefebvre E, Rousseau J-P, Burgy F and Malka V 2004 A laser–plasma accelerator producing monoenergetic electron beams *Nature* **431** 541
[11] Jaroszynski D A *et al* 2006 Radiation sources based on laser–plasma interactions *Phil. Trans. R. Soc.* A **364** 689
[12] Schlenvoigt H-P *et al* 2008 A compact synchrotron radiation source driven by a laser–plasma wakefield accelerator *Nat. Phys.* **4** 130
[13] Wen M, Tamburini M and Keitel C H 2019 Polarized laser-wakefield-accelerated kiloampere electron beams *Phys. Rev. Lett.* **122** 214801
[14] Wu Y *et al* 2019 Polarized electron-beam acceleration driven by vortex laser pulses *New J. Phys.* **21** 073052
[15] Büscher M, Hützen A, Ji L and Lehrach A 2020 Generation of polarized particle beams at relativistic laser intensities *High Power Laser Sci. Eng.* **8** e36
[16] Rathmann F, Saleev A and Nikolaev N N 2014 Search for electric dipole moments of light ions in storage rings *Phys. Part. Nuclei* **45** 229
[17] Moortgat-Pick G *et al* 2008 Polarized positrons and electrons at the linear collider *Phys. Rep.* **460** 131
[18] Burkardt M, Miller C A and Nowak W-D 2009 Spin-polarized high-energy scattering of charged leptons on nucleons *Rep. Prog. Phys.* **73** 016201
[19] Ageev E *et al* 2005 Measurement of the spin structure of the deuteron in the DIS region *Phys. Lett.* B **612** 154
[20] Glashausser C 1979 Nuclear physics with polarized beams *Annu. Rev. Nucl. Part. Sci.* **29** 33
[21] Jaffe R L 2003 Open questions in high energy spin physics *Int. J. Mod. Phys.* A **18** 1141
[22] Adlarson P *et al* 2014 Evidence for a new resonance from polarized neutron–proton scattering *Phys. Rev. Lett.* **112** 202301
[23] Baer H *et al* 2013 The International linear collider technical design report-volume 2: physics (arXiv:1306.6352)
[24] Gay T J 2009 Chapter 4 physics and technology of polarized electron scattering from atoms and molecules *Adv. At. Mol. Opt. Phys.* **57** 157
[25] McDaniel E W 1982 *Applied Atomic Collision Physics: A Treatise in Five Volumes. Gas Lasers/Volume* ed E W McDaniel and W L Nighan (London: Academic)
[26] An X Y, Chen M, Li J X, Weng S M, He F, Sheng Z M and Zhang J 2019 Mapping electromagnetic fields structure in plasma using a spin polarized electron beam *Phys. Plasmas* **26** 123106
[27] Raab N *et al* 2014 Polarization measurement of laser-accelerated protons *Phys. Plasmas* **21** 023104
[28] Li X F, Gibbon P, Hützen A, Büscher M, Weng S M, Chen M and Sheng Z M 2021 Polarized proton acceleration in ultraintense laser interaction with near-critical-density plasmas *Phys. Rev.* E **104** 015216
[29] Mane S R, Shatunov Y M and Yokoya K 2005 Spin-polarized charged particle beams in high-energy accelerators *Rep. Prog. Phys.* **68** 1997
[30] Sokolov A A and Ternov I M 1967 Synchrotron radiation *Sov. Phys. J.* **10** 39
[31] Guo R-T, Wang Y, Shaisultanov R, Wan F, Xu Z-F, Chen Y-Y, Hatsagortsyan K Z and Li J-X 2020 Stochasticity in radiative polarization of ultrarelativistic electrons in an ultrastrong laser pulse *Phys. Rev. Res.* **2** 033483
[32] Chen Y-Y, He P-L, Shaisultanov R, Hatsagortsyan K Z and Keitel C H 2019 Polarized positron beams via intense two-color laser pulses *Phys. Rev. Lett.* **123** 174801
[33] Seipt D, Del Sorbo D, Ridgers C P and Thomas A G 2019 Ultrafast polarization of an electron beam in an intense bichromatic laser field *Phys. Rev.* A **100** 061402
[34] Del Sorbo D, Seipt D, Blackburn T G, Thomas A G, Murphy C D, Kirk J G and Ridgers C 2017 Spin polarization of electrons by ultraintense lasers *Phys. Rev.* A **96** 043407
[35] Li Y-F, Shaisultanov R, Hatsagortsyan K Z, Wan F, Keitel C H and Li J-X 2019 Ultrarelativistic electron-beam polarization in single-shot interaction with an ultraintense laser pulse *Phys. Rev. Lett.* **122** 154801

[36] Wu Y *et al* 2020 Spin filter for polarized electron acceleration in plasma wakefields *Phys. Rev. Appl.* **13** 044064

[37] Wen M, Keitel C H and Bauke H 2017 Spin-one-half particles in strong electromagnetic fields: spin effects and radiation reaction *Phys. Rev.* A **95** 042102

[38] Wu Y *et al* 2019 Polarized electron acceleration in beam-driven plasma wakefield based on density down-ramp injection *Phys. Rev.* E **100** 043202

[39] Hützen A *et al* 2019 Polarized proton beams from laser-induced plasmas *High Power Laser Sci. Eng.* **7** e16

[40] Sofikitis D, Kannis C S, Boulogiannis G K and Rakitzis T P 2018 Ultrahigh-density spin polarized H and D observed via magnetization quantum beats *Phys. Rev. Lett.* **121** 083001

[41] Vieira J, Huang C-K, Mori W and Silva L 2011 Polarized beam conditioning in plasma based acceleration *Phys. Rev. Spec. Top.* **14** 071303

[42] Sadighi-Bonabi R and Rahmatallahpur S 2010 Potential and energy of the monoenergetic electrons in an alternative ellipsoid bubble model *Phys. Rev.* A **81** 023408

[43] Wu H-C, Xie B-S, Zhang S, Hong X-R, Zhao X-Y and Liu M-P 2010 Bubble core field modification by residual electrons inside the bubble *Phys. Plasmas* **17** 113103

[44] Li X F, Yu Q, Gu Y J, Huang S, Kong Q and Kawata S 2015 Bubble shape and electromagnetic field in the nonlinear regime for laser wakefield acceleration *Phys. Plasmas* **22** 083112

[45] Li X F, Gu Y J, Yu Q, Huang S, Zhang F, Kong Q and Kawata S 2014 Dependence of electron trapping on bubble geometry in laser–plasma wakefield acceleration *Phys. Plasmas* **21** 073109

[46] Chitgar Z M, Gibbon P, Böker J, Lehrach A and Büscher M 2020 Electron self-injection threshold for the tandem-pulse laser wakefield accelerator *Phys. Plasmas* **27** 023106

[47] Qu J F, Li X F, Liu X Y, Liu P, Song Y J, Fu Z, Yu Q and Kong Q 2019 Terahertz radiation generated by shell electrons in the bubble regime via the interaction between an intense laser and underdense plasma *Phys. Plasmas* **26** 033115

[48] Assmann R *et al* 2020 EuPRAXIA conceptual design report *Eur. Phys. J. Spec. Top.* **229** 3675

[49] Arber T D *et al* 2015 Contemporary particle-in-cell approach to laser–plasma modelling *Plasma Phys. Control. Fusion* **57** 113001

[50] Kostyukov I, Pukhov A and Kiselev S 2004 Phenomenological theory of laser–plasma interaction in 'bubble' regime *Phys. Plasmas* **11** 5256

[51] Lu W, Huang C, Zhou M, Mori W B and Katsouleas T 2006 Nonlinear theory for relativistic plasma wakefields in the blowout regime *Phys. Rev. Lett.* **96** 165002

[52] Lu W, Tzoufras M, Joshi C, Tsung F, Mori W, Vieira J, Fonseca R and Silva L 2007 Generating multi-GeV electron bunches using single stage laser wakefield acceleration in a 3d nonlinear regime *Phys. Rev. Spec. Top.* **10** 061301

[53] Schnell M *et al* 2013 Optical control of hard x-ray polarization by electron injection in a laser wakefield accelerator *Nat. Commun.* **4** 1

[54] Thomas J, Hützen A, Lehrach A, Pukhov A, Ji L, Wu Y, Geng X and Büscher M 2020 Scaling laws for the depolarization time of relativistic particle beams in strong fields *Phys. Rev. Accel. Beams* **23** 064401

[55] Büscher M, Adam R, Tusche C, Hützen A, Wiemann C, Chen Y-J and Schneider C M 2020 JuSPARC—the Jülich short-pulsed particle and radiation center *J. Large-Scale Res. Fac.* **6** 138